Curve fitting complex X-ray photoelectron spectra of graphite-supported copper nanoparticles using informed line shapes

Vincent Fernandez, Daniyal Kiani, Neal Fairley, Francois-Xavier Felpin, Jonas Baltrusaitis

Curve Fitting Complex X-ray Photoelectron Spectra of Graphite-Supported Copper Nanoparticles Using Informed Line Shapes

Vincent Fernandez,[1] Daniyal Kiani,[2] Neal Fairley,[3] François-Xavier Felpin,[1] and Jonas Baltrusaitis,[2,*]

[1]Institut des Matériaux Jean Rouxel, 2 rue de la Houssinière, BP 32229, F-44322 Nantes Cedex 3, France

[2]Department of Chemical and Biomolecular Engineering, Lehigh University, 111 Research Drive, Bethlehem, PA 18015, USA

[3]Casa Software Ltd, Bay House, 5 Grosvenor Terrace, Teignmouth, Devon TQ14 8NE, UK

Abstract

Complex spectral envelopes of transition metal photo-excitations obtained using X-ray Photoelectron Spectroscopy (XPS) contain extensive information on the oxidation states and chemical bonding but pose multiple challenges for extracting reliable data due to the presence of multiple closely lying binding energy peaks. In this work, we outlined a procedure for graphite supported copper nanoparticles (Cu NP/graphite) XPS data interpretation that involves constructing spectral envelopes of the potential copper components (Cu_2O, CuO and $Cu(OH)_2$) extracted from the diverse set of Cu NP/graphite samples and using Linear Least Squares (LLS) fitting to reconstruct the exact surface composition of Cu NP/graphite samples. We utilized Informed Amorphous Sample Model (IASM) to calculate spectral envelopes using a physical process affecting the series of Cu NP/graphite samples, namely their synthesis procedure, to construct an informed line shape necessary to complete data reproduction by the model. The method described herein can be used to interpret crucial XPS data obtained in many science and engineering disciplines, including chemistry, fundamental and applied surface science, catalysis, semiconductors and many others. A brief discussion is also provided on the opportunities and pitfalls of deriving standard model line shapes from user sourced online databases.

*corresponding author: job314@lehigh.edu; +1-610-758-6836

keywords: X-ray photoelectron spectroscopy; spectral envelope; copper nanoparticles, graphite, data driven spectral analysis

1. **Introduction**. Elemental and chemical state analysis by X-ray Photoelectron Spectroscopy (XPS) is an important tool in surface science and technology [1]. Reproducibility and reliability of this technique are underpinned by verifiable characterization of instrumentation so that results obtained by XPS are understandable, repeatable and scientifically beneficial. Interpretation of data, especially complex spectral envelopes of the transition metals [2–7], requires complex peak fitting procedures using synthetic components and subtraction of the background due to the inelastically scattered electrons. Purely synthetic components always involve a certain arbitrariness in choosing line shape parameters and the contributing number of spectral components. Hence, this typically involves a trial and error process with adjustments made to peak and background parameter constraints and line shape. The line shapes selected are very influential in the outcome in terms of relative peak integrated intensities and are therefore an important choice when fitting a data envelope. Commonly accepted Gaussian instrumental broadening in addition to the Lorentzian energy distribution of the electrons often govern the mixed Gaussian-Lorentzian peak shape [8] while asymmetry within a line shape is often required [9] but less used. Without guidance from the data itself for the selection of the asymmetry parameters, it is extremely difficult to make a choice that would be significant to the outcome. For this reason, these final peak models are often *ad hoc* in nature. Because of not using any appropriate guidance about the structural, physical and chemical processes affecting the sample, subjective data interpretation and quantification are often obtained. A vector-based Informed Amorphous Sample Model (IASM) [10] was recently developed to provide an alternative to XPS spectra fitting that effectively reduced arbitrariness by incorporating information about a physical process affecting the sample without the need to identify synthetic line shapes. Instead, the spectral forms are extracted using the external modifiers to the sample, such as heat or X-ray degradation, which introduce a shape constraint for a guided synthetic line shape necessary to complete data reproduction by the model.

XPS analysis of supported metal nanoparticles [11] provides detailed information on their electronic (surface) structure as a function of size and how surface atom coordination impacts the electronic structure as well as the specific functional properties. Specifically, supported copper nanoparticles have been shown to perform many hydrocarbon and oxygenate conversion reactions due to the presence of the specific reduced sites. For example, copper catalysts are known to hydrogenate furfural and the presence of both Cu(0) and Cu(I) sites is necessary [12]. Carbon dioxide electrochemical reduction in liquid environments to form

hydrocarbons proceeds exclusively on copper catalysts [13,14]. Carbon dioxide was electrochemically reduced towards ethylene through facile and tunable plasma treatments and Cu(I) sites were shown to be active [15]. Other work showed metallic Cu(0) to be active sites for the same reaction [16] via means of *ex situ* XPS. Hence, Cu(0) and Cu(I) sites are routinely observed in various catalyst materials and the relative ratios of these two species are obtained by peak fitting and integrating the two peaks at ~916.0 and ~918.3 eV and taking the ratio of the respective areas [17]. This method can potentially introduce significant errors due to the (a) proximity of the Cu $2p_{3/2}$ peaks for these oxidation states and (b) *in situ* operating environments introducing other species due to the gas phase molecules [18]. New developments in instrumentation and electronics enabling X-ray spectroscopy under elevated gas pressures up to near ambient (NAP-XPS) [19,20] further provide for the ability of the complex metal or metal oxide particle analysis under gas atmosphere and temperature conditions relevant to those found in experiments [21–25]. This expanded XPS use into studies of solid-gas, solid-liquid, and vapor-liquid interfaces with applications including environmental chemistry, catalysis, and CO_2 electrochemistry [26–31]. **Figure 1** shows that Cu $2p_{3/2}$ peak binding energy data for $Cu(OH)_2$ and CuO overlap and may lead to the assignment errors in NAP-XPS data. A significant overlap between Cu and Cu_2O is also observed due to the proximity of the Cu $2p_{3/2}$ peaks while $Cu(OH)_2$ is also present in moist environments but rarely identified. Improved XPS data processing methods are needed for accurate evaluation of copper elemental and chemical state analysis. A recent review by Sherwood provides an excellent tutorial towards the peak fitting of the XPS data [32] and suggests a guess of the fitting parameters needs to be made based upon a good understanding of the chemistry and physics of the surface under study. This guess needs to take into account related and existing data for similar systems or samples, including valuable information available in the database and comparative tools including a selection of the number of peaks present, together with a guessed value for the parameters that define each peak [32]. In complex heterogeneous environments, the selection of these parameters becomes arbitrary and is often guided by the interpreter's bias [10].

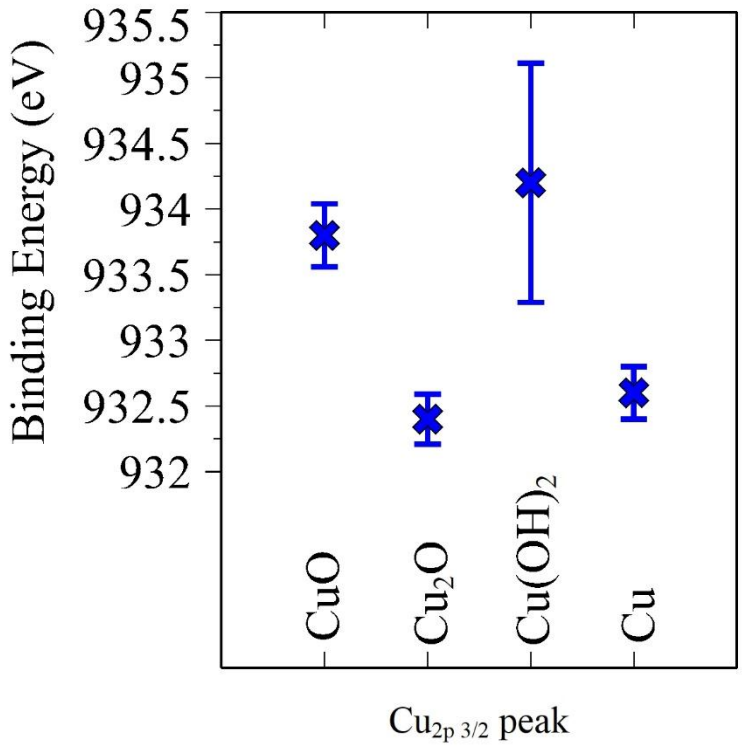

Figure 1. Compiled Cu $2p_{3/2}$ peak binding energy data for Cu, $Cu(OH)_2$ Cu_2O and CuO. A significant overlap between $Cu(OH)_2$ and CuO as well as Cu and Cu_2O can be observed. The error bars represent the standard deviation between all reported values, obtained from references. Individual references and corresponding data are summarized in **Table S1.**

In this work, we report developments in XPS analysis of copper particles supported on graphite (Cu NP/graphite) aimed at providing an operating mode capable of delivering the sensitivity and energy resolution suitable for most practical application of chemical state analysis while maintaining identical uniform response of intensity to electron energy. In particular, identification of the chemical shifts and oxidation states in complex spectral envelopes, such as those of Cu 2p where shake-up and multiplet split contributions yield very complex line shapes, is difficult and a holistic approach is often taken where Auger and valence bands regions are also inspected simultaneously [33]. There is also the concern that surface sensitivity changes with kinetic energy for transition metal oxides with potential surface contamination envelopes that typically span for tens of eV and encompass steep change due to the inelastically scattered background. Well-formed photoemission lines need to be modeled by asymmetric line shapes to separate close-lying oxidation states, such as those of Cu(0) and Cu(I) [34]. Initially, we show the performance of the calibrated XPS instrument which allows defining the FWHM of the peaks necessary for fitting. We then perform peak fitting of the data where we extract synthetic components of graphite, Cu_2O,

CuO and $Cu(OH)_2$ from the existing data and use them to interpret any related components of the similar systems using Cu NP/graphite as an example. For this, a combination of IASM model [10] and Linear Least Squares is utilized.

2. Experimental

2.1. Graphite supported copper nanoparticle (Cu/graphite) synthesis. Synthesis method has been described previously [33]. Briefly, copper acetate monohydrate (0.1 g, 0.5 mmol) was dissolved in degassed methanol (60 mL) at 25 °C. Graphite (0.5 g, <20 μm particle size, Aldrich) was added and the solution was degassed 5 min with H_2. The solution was stirred for 16 h under H_2 atmosphere at 25 °C. The solid was collected by filtration, washed with distilled methanol (3 × 5 mL), deionized water (3 × 5 mL), acetone (3 × 5 mL) then dried under vacuum overnight to give a black solid. ICP-MS analysis determined that the content of copper onto graphite was ca. 4.8–5 wt. %. Synthesis conditions are shown in **Table 1**.

Table 1. Synthesis conditions and sample labeling of the Cu NP/graphite samples used in XPS studies.

Cu NP/graphite	Preparation method	Synthesis time, hours	Synthesis temperature, °C	Loading on support, % weight	Particle shape[a]	Particle size range, nm[a]	Average size, nm[a]
TM07	$NaBH_4$ in H_2O	12	80	20	spherical	8-9	8.6
TM09	hydrazine in MeOH	24	Under reflux	20	spherical	20-200	97
TM10	hydrazine in H_2O	24	Under reflux	20	cubic	100-400	234
TM15	calcination	3	350	20	spherical	20-30	25
TM17	H_2 in MeOH	12	25	5	spherical	2-3	2.2
TM18	H_2 in MeOH, then calcination	12 + 3	25 then 350	5	spherical	10-15	12
TM19	H_2 in H_2O	12	25	20	uncontroled	100-400	316

a. Particle size and shape were determined from Transmision Electron Microscopy (TEM) measurements. From 30 to 200 particles were measured in each case.

2.2. XPS analysis and data processing.

2.2.1. XPS sample measurements. X-ray photoelectron spectroscopy (XPS) analysis was performed using Kratos Axis Nova and Ultra (University of Nantes, Nantes, France) instruments. The instrument used a monochromated Al Kα source 1486.6 eV. The instrument base pressure was 5 x 10^{-10} Torr. The instrument calibration was done following the procedure by Seah *et al*. [35,36]. The slot aperture was used for survey spectra with an analysis area of ca.700 um x 300 μm, while a 27 μm selected area aperture was used for high-resolution regions. Pass energy (PE) of 80 eV, corresponding to an all over Fermi edge resolution of 0.89 ± 0.02 eV with a 0.5 eV step, was used to acquire wide range survey spectra. A PE of 20 eV, corresponding to an all over Fermi edge resolution of 0.40 ± 0.02 eV with a 0.1 eV step, was used to acquire narrow spectra of the Cu 2p, C 1s orbitals and valence band region. The carbon conductivity was good enough to avoid any charging artifacts. All measurements were performed without charge neutralizer. TM samples used to create the LLS solutions were measured using 300W X-ray power. For the degradation study of TM15, the X-ray power was 150W. The PE160 survey measurement returned 284.3 eV for C 1s peak calibration.

2.2.2. Tougaard background. The Tougaard background [37] is computed from the measured spectrum $S(E)$ generated by the photoemission peak plus inelastic scattering signal due to the photoemission peak using the integral

$$T(E) = \int_E^\infty F(E' - E)S(E')dE' \quad (1)$$

where

$$F(x) = \frac{Bx}{(C-x^2)^2+Dx^2} = B\frac{x}{(C-x^2)^2+Dx^2} = B \times G(x) \quad (2)$$

Therefore

$$T_n(E) = \int_E^\infty G(E' - E)S(E')dE' \quad (3)$$

$$T(E) = BT_n(E) \quad (4)$$

If the start energy for the region over which the background is defined is E_s , then the value B is calculated such that

$$S(E_s) - Start\ Offset = T(E_s) \quad (5)$$

so that

$$B = \frac{S(E_s)-Start\ Offset}{T_n(E_s)} \quad (6)$$

where $Start\ Offset$ is the offset defined in the region parameter in CasaXPS.

The U 2 Tougaard background used in this paper is formed from the above definition by setting D = 0 and using a negative value for the C parameter in Equation (2).

2.2.3. Linear Least Squares Approximation. Given a set of linearly independent functions $\{f_1(x), \quad f_2(x), \quad f_3(x), \dots, f_m(x)\}$ a function $y(x)$can be defined by

$$y(x) = c_1 f_1(x) + c_2 f_2(x) + c_3 f_3(x) + \cdots + c_m f_m(x) \quad \dots \qquad (7)$$

where $c_1, c_2, c_3, \dots, c_m$ are constant values.

In a well-posed example the list of functions $\{f_1(x), \quad f_2(x), \quad f_3(x), \dots, f_m(x)\}$ are component-curves differing in position (defined by peak maximum) and shape. The weighted sum of these component spectra $y(x)$ represents a linear least squares solution approximating a measured data envelope.

When using Equation (1) to model a spectrum, the function $y(x)$ must reproduce the data envelope *as closely as possible*. The concept expressed by the term *closely* has the mathematical meaning as follows. The conventional and common measure of closeness is the least-squares sum

$$L(c_1, c_2, c_3, \dots, c_m) = \sum_{i=1}^{n} (y(x_i) - d_i)^2 \quad \dots \qquad (8)$$

is a minimum, where $\{d_1, d_2, d_3, \dots, d_n\}$ are n data channels in which signal is collected representing intensity partitioned by incrementing binding energy.

Minimizing the function $L(c_1, c_2, c_3, \dots, c_m)$ with respect to the parameters $c_1, c_2, c_3, \dots, c_m$ is achieved by requiring

$$\frac{\partial L}{\partial c_j} = 0 \; for \; all \; j = 1,2,3, \dots, m \qquad (9)$$

Since

$$L(c_1, c_2, c_3, \dots, c_m) = \sum_{i=1}^{n} (c_1 f_1(x_i) + c_2 f_2(x_i) + c_3 f_3(x_i) + \cdots + c_m f_m(x_i) - d_i)^2 \qquad (10)$$

$$\frac{\partial L}{\partial c_j} = \sum_{i=1}^{n} 2 f_j(x_i)(c_1 f_1(x_i) + c_2 f_2(x_i) + c_3 f_3(x_i) + \cdots + c_m f_m(x_i) - d_i) = 0 \qquad (11)$$

Collecting terms are rearranging the minimization problem yields the following.

$$\sum_{i=1}^{n} f_j(x_i)\big(c_1 f_1(x_i) + c_2 f_2(x_i) + c_3 f_3(x_i) + \cdots + c_m f_m(x_i)\big) = \sum_{i=1}^{n} f_j(x_i) d_i \qquad (12)$$

$$c_1 \sum_{i=1}^{n} f_j(x_i) f_1(x_i) + c_2 \sum_{i=1}^{n} f_j(x_i) f_2(x_i) + c_3 \sum_{i=1}^{n} f_j(x_i) f_3(x_i) + \dots + c_m \sum_{i=1}^{n} f_j(x_i) f_m(x_i) = \sum_{i=1}^{n} f_j(x_i) d_i \qquad (13)$$

If we use vector notation $\boldsymbol{v_j} = \left(f_j(x_1), f_j(x_2), f_j(x_3), \dots, f_j(x_n)\right)$ and $\boldsymbol{d} = (d_1, d_2, d_3, \dots, d_n)$ then, using dot product notation for vector scalar multiplication, the condition for minimizing the function $L(c_1, c_2, c_3, \dots, c_m)$ reduces to a system of linear equations in m unknowns the solution of which yields a function $y(x)$ that approximates data $\{d_1, d_2, d_3, \dots, d_n\}$ in a least squares sense. These linear equations can be written as follows:

$$\begin{aligned} c_1\boldsymbol{v_1}.\boldsymbol{v_1} + c_2\boldsymbol{v_1}.\boldsymbol{v_2} + c_3\boldsymbol{v_1}.\boldsymbol{v_3} + \cdots + c_m\boldsymbol{v_1}.\boldsymbol{v_m} &= \boldsymbol{v_1}.\boldsymbol{d} \\ c_1\boldsymbol{v_2}.\boldsymbol{v_1} + c_2\boldsymbol{v_2}.\boldsymbol{v_2} + c_3\boldsymbol{v_2}.\boldsymbol{v_3} + \cdots + c_m\boldsymbol{v_2}.\boldsymbol{v_m} &= \boldsymbol{v_2}.\boldsymbol{d} \\ c_1\boldsymbol{v_3}.\boldsymbol{v_1} + c_2\boldsymbol{v_3}.\boldsymbol{v_2} + c_3\boldsymbol{v_3}.\boldsymbol{v_3} + \cdots + c_m\boldsymbol{v_3}.\boldsymbol{v_m} &= \boldsymbol{v_3}.\boldsymbol{d} \quad \dots \\ &\vdots \\ c_1\boldsymbol{v_m}.\boldsymbol{v_1} + c_2\boldsymbol{v_m}.\boldsymbol{v_2} + c_3\boldsymbol{v_m}.\boldsymbol{v_3} + \cdots + c_m\boldsymbol{v_m}.\boldsymbol{v_m} &= \boldsymbol{v_m}.\boldsymbol{d} \end{aligned} \tag{14}$$

If a matrix $\boldsymbol{A}$ is defined in terms of the vectors $\boldsymbol{v_j}$

$$\boldsymbol{A} = [\boldsymbol{v_1}, \boldsymbol{v_2}, \boldsymbol{v_3}, \dots, \boldsymbol{v_m}] \tag{15}$$

Then the set of simultaneous equations written in matrix notation becomes

$$A^T A c = A^T d \tag{16}$$

where $\boldsymbol{c} = (c_1, c_2, c_3, \dots, c_m)$. The least-squares problem has a theoretical solution, provided the inverse matrix $(\boldsymbol{A^T A})^{-1}$ exists, in the form

$$c = (A^T A)^{-1} A^T d \quad \dots \tag{17}$$

Equation (17) is solved by computing the inverse matrix $(\boldsymbol{A^T A})^{-1}$ by means of the singular value decomposition algorithm described in Béchu *et al*. [38]. Non-negative constraints are applied to the fitting of spectral forms to data as part of the linear least-squares procedure.

2.2.4. Informed Amorphous Sample Model (IASM) for data analysis via spectral components. IASM was used to extract fitting spectral components from a set of experimental data [10]. These components are non-synthetic and not arbitrarily chosen, but rather extracted from experimental data and are informative of the physical nature of the sample. The data processing involved (1) identification of a subset of spectra that can be mathematically described using only two principal components or spectral forms and (2) reproduction of the entire data subset by using linear combinations of these two spectral forms only. The first step uses a standard linear Principal Component Analysis (PCA) procedure while the second step uses standard linear least-squares fitting to find the

appropriate spectral forms that can be used as components in a peak model. The exact data processing steps were as follow.

1. It was assumed graphite was the dominant source for C 1s signal and all samples contained spectra and background compatible with a graphitic signal,
2. A contribution from graphitic signal was removed from spectra measured from each TM sample by computing a value for C 1s intensity above a U 2 Tougaard background, where identical Tougaard cross-section parameters are used for graphite and TM samples, then a proportion of graphite spectra calculated as the ratio of C $1s_{TM}$ to C $1s_{graphite}$ is subtracted from each TM sample.,
3. Since graphite spectra contribute O 1s signal to TM spectra and the exact nature of O 1s signal from graphite from different TM samples is unknown at the time of removing the graphitic contribute from TM samples, a pre-processing step is performed to eliminate O 1s from the reference graphite data. A linear background was placed beneath the O 1s peak measured from graphite and the background for the energy interval defined for the O 1s peak replaces the measured O 1s peak for graphite. This is deemed preferable to subtracting O 1s based on the standard graphite data, but should be allowed for when copper and oxygen is compared in computed spectra,
4. The act of subtracting graphitic signal has greatest influence on the valance band (VB) data hence a subtraction procedure is required to unveil copper chemical information within VB data. A comparison of computed VB spectra to standard Cu (I) and Cu(II) oxide is important to data analysis,
5. The C 1s narrow scan region is omitted from spectra analyzed. The rationale for omitting the C 1s region is related to the narrow width for graphitic C 1s and the relatively intense signal for C 1s compared to copper which is anticipated to create a bias in linear least squares reproduction steps used as part of the analysis of TM samples. Broader loss peaks from C 1s are included in the calculation to support and guide linear least squares to a meaningful graphitic contribution within TM data.
6. An important feature for these data is the use of graphitic support. Alignment of the graphitic C 1s peak through TM samples is assumed to imply a common binding energy scale for all measurements. No binding energy calibration is performed for TM samples analyzed,
7. Vector decomposition is performed making use of TM17, TM09 and the degradation sequence based on TM15. TM17 is predominately hydroxide in nature. TM15 is

initially predominately Cu(II) oxide whereas TM09 contains a significant proportion of Cu(I) oxide. From these data a total of three copper spectral forms are computed which are supplemented with the graphite spectral form as described above,

8. Linear least-squares solutions to TM samples are used to partition signal between different chemical states of copper.

2.2.5. Data processing software. XPS data including peak fitting, line shape synthesis, envelope background modeling and subtraction, quantification of components and plotting, was processed using a *CasaXPS* program (suite version 2.3.23).

3. Results and discussion.

3.1. Challenges associated with the assignment of Cu 2p photoemission peaks in copper particles. There are many samples analyzed by XPS where the concept that to each chemical state within a peak model there is a component peak that can be identified with a chemical state. While for many samples the one-chemical-state one-component approach is adequate, there are however many examples where this approach is of limited use. Copper and copper oxides exhibit both simple and complex structure providing examples for the fitting of peaks to data where the difficulty is evident for different reasons in both the simple single-component case and also in the complex peak structure case.

For an isolated copper atom, the ground state electron configuration can be viewed as

$$1s^2 2s^2 2p^6 3s^2 3p^6 3d^{10} 4s^1 = [\mathrm{Ar}] 3d^{10} 4s^1$$

When in the solid-state, the XPS of copper results in spectroscopic features depending on how compounds make use of valence electrons $3d^{10}4s$ with both significant and insignificant differences in core-level photoemission peaks depending on oxidation state. Only by comparing valence band and Auger spectra is it possible to distinguish between metallic copper Cu(0) and Cu_2O Cu(I). Photoemission from Cu 2p and Cu 3p for these Cu(0) and Cu(I) are highly correlated in terms of binding energy and peak shape, whereas there is a dramatic change to these photoemission peaks for Cu(II) oxidation state. These Cu(II) spectra demonstrate how photoemission peaks do not necessarily conform to the concept of well-defined peaks that can easily be approximated by a single component within a peak model representing a chemical state for said material. Rather than one-to-one correspondence between component peaks and chemical states, copper provides examples of where XPS yields spectral signatures for chemical state spread over many eV. Separation of chemical state signal based on these types of data envelopes remains a goal for XPS, but assigning

binding energy to specific features with these extended structures is not as important or appropriate as the intrinsic shape that conveys the identity for oxidation state. **Figure 2** displays Cu 2p doublet peaks that (1) spread over an energy interval of more than 30 eV and (2) illustrates the changes possible for spectra where incomplete electron shells result in complex structures not easily open to interpretation by individual components within a peak model. Cu(II) is complicated by the possibility that a characteristic spectral shape is a consequence of both CuO and $Cu(OH)_2$ both contributing to the observed data.

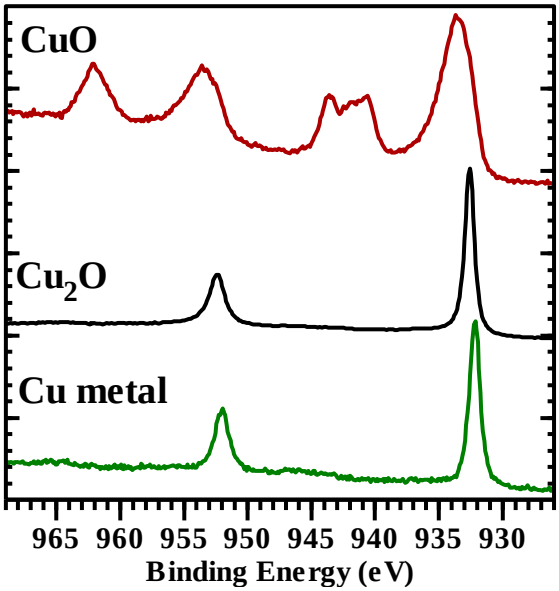

Figure 2: Copper metal and oxide spectra illustrating a similarity between Cu 2p for Cu(0) and Cu(I) (Cu_2O) while Cu(II) (CuO) takes a form dictated to by multiplet splitting for a material where both d and s orbitals contribute to the oxide signal formation. The binding energy for Cu(I) and Cu(II) is not well defined as both were measured using charge compensation.

In this work, we make use of copper supported on graphite as a means of investigating copper oxidation states by developing IASM components. Graphite C 1s signal is used for confirming binding energy calibration for recorded spectra. Data treatment by IASM makes use of linear analysis and therefore confidence in the energy calibration is essential.

3.2. Copper nanoparticles supported on graphite: determining instrumental parameters using a well-defined C 1s region. Data measured from a set of samples synthesized using the procedure described by d'Halluin *et al*. [33] from C 1s spectra show that graphitic signal can be used to characterize and align spectra from different copper oxidation states for copper nanoparticles supported on graphite. While the line shape for pass energy 160 slot is far from ideal, intensity and transmission characteristics for this mode allowing quantification are not compromised by factors influencing line shapes. High

sensitivity modes are an essential part of the analysis by XPS and these data from graphite provide evidence quantification is possible making use of the flat transmission response to imaging lens mode FoV2 pass energy of 160 full slot selected area aperture. Survey data presented in **Figure 3** is quantified using the C 1s signal and C KLL Auger emission. Both peak areas are corrected for escape depth only [39]. Relative sensitivity for these two peaks for low atomic number atoms is linked in the sense that photoemission from the K shell is directly linked to Auger emission [40] as the dominant relaxation mode for carbon. The angular distribution is identical for C 1s and C KLL. This was verified by the fact that the quantification between F1s and F2s showed 50/50% based on Effective Attenuation Length (EAF) and Scofield cross-sections [41–43]. **Figure 3 inset** presents C 1s spectra measured using 27 μm slot selected area aperture mode and pass energy of 5. Combining improved energy resolution from pass energy of 5 and narrow width of signal due to the 27 μm slot, selected area aperture yields data from graphite and two sample of Cu NP/graphite – TM07 and TM10 - with identical peak shape. These data show no alteration to peak position, FWHM or shape for C 1s spectra. These data provide evidence supporting the use of graphitic signal in data treatment used to analyze Cu oxidation state of Cu NP/graphite by d'Halluin *et al*. [33].

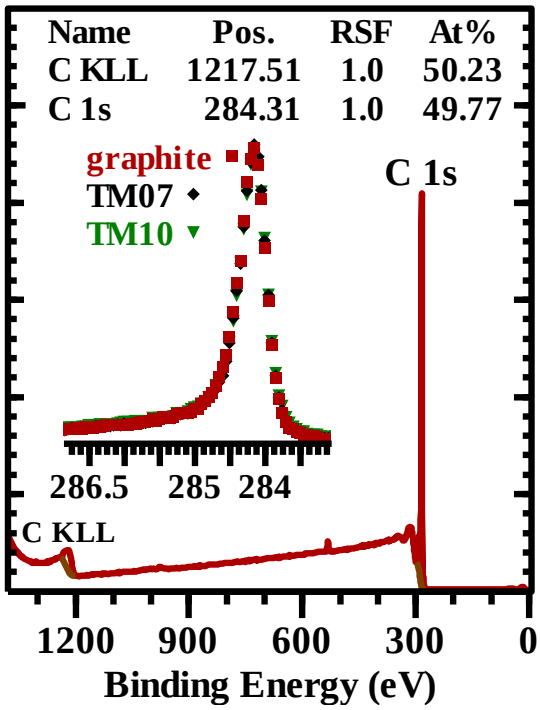

Figure 3. **Survey data measured from graphite using pass energy 160 full slot selected area aperture. (inset) Comparison of graphite and two Cu NP/ graphite samples containing graphite measured using pass energy of 5 eV and making use of the 27 μm slot selected area aperture mode.**

3.3. Copper nanoparticles supported on graphite: deriving spectral envelopes to separate the copper signal. We begin by illustrating the complex problem of accurately describing the oxidation states of copper. Routinely, it is done by peak fitting Cu 2p region

with synthetic components. Provided with the complexity of using Cu 2p region only, we turn to the overall spectral envelope. **Figure 4** shows Cu 3p and valence band region spectra of Cu metal and Cu_2O. Cu 3p doublet of Cu_2O peaks look very similar to those of Cu metal, but the valence associated with the Cu_2O components is clearly different from the metallic Cu valence band. This illustrates how Cu 3p and valence band data support the assignment of Cu_2O rather than Cu metal. Additionally, the data shown in **Figure 4** were obtained without charge compensation from TM experimental samples implying that the graphite substrate has played a significant role in establishing the correct energy scale needs to be accounted for when computing IASM spectral envelopes.

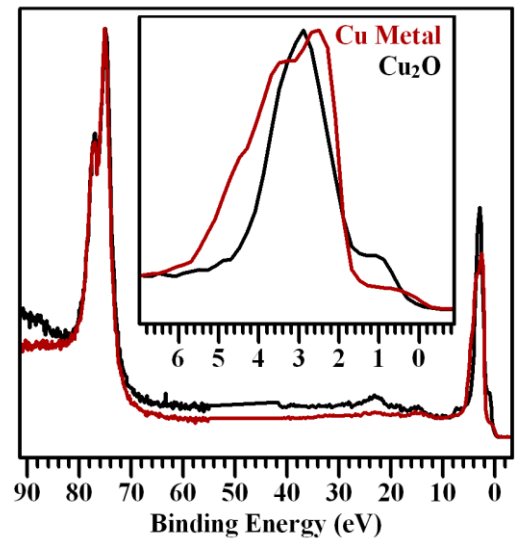

Figure 4. **Cu 3p and valence band region spectra of Cu metal and Cu_2O extracted from TM samples**.

Following the logic established in **Figure 4**, three spectral components of copper compounds were constructed from samples TM09, TM19 and TM17 using IASM method [10]. Additionally, graphite fitted to TM09 (mostly Cu_2O) and TM19 (mostly CuO and $Cu(OH)_2$). These spectral components were constructed for Cu 3p and valence band spectra only and no Cu 2p region was used. For component extraction, we considered the evolution in spectral shapes due to the synthesis procedure variation within the TM set of samples. The data processing involved identification of a subset of spectra that can be mathematically described using only two principal components or spectral forms and reproduction of the entire data subset by using linear combinations of these two spectral forms only. Notably, the spectral forms **identified** must exhibit contrast due to a physical or chemical process. If they are not *sufficiently different*, the optimization procedure will not return a well-defined solution. In this case, three copper oxide and hydroxide components were identified including Cu_2O, CuO and $Cu(OH)_2$). The spectral components obtained are shown in **Figure 5**.

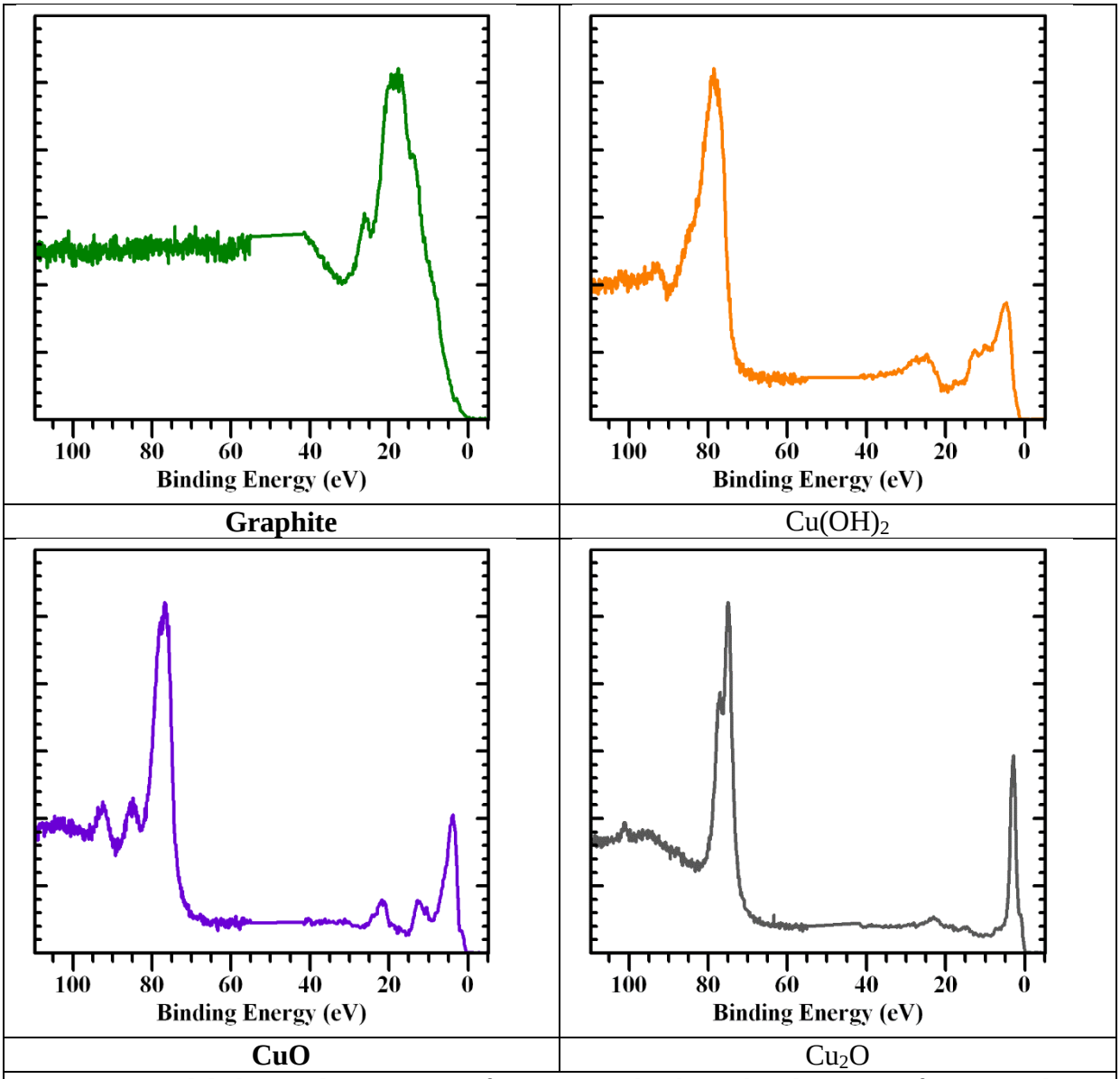

Figure 5. Model chemical components for Cu 3p and valence band regions of TM samples into four components. These components are standard spectra from graphite plus three computed components from samples TM09, TM17 and TM19.

Utilizing the spectral components shown in **Figure 5**, spectral fitting was performed to determine the composition of the TM09, TM18 and TM19 samples. Effectively, LLS spectra shown in black illustrates a spectrum formed from the sum of a set of four spectra representing different elemental (carbon and copper) and different chemical state for copper appropriately scaled to reproduce a spectrum measured from samples. It can be seen that LLS derived spectra almost fully overlap with the experimental spectra, now providing an exact composition of each component contributing to it. These compositions are compiled in **Table 2**. No metallic Cu was observed on the surface of these particles as they form a

complex oxide or hydroxide layers under moist environments. From the results shown in **Figure 6,** it can be inferred that hydrazine in methanol is an efficient reagent to deposit partially reduced Cu NP on graphite as manifested by a relatively high Cu_2O content, as compiled in **Table 2**. Further, NP dispersion can influence the observed spectral intensity [44] while the particle size could influence the Cu 2p spectrum via variation in the relative peak area intensities of the shake-up lines [45]. Correlation between the synthesized particle structural parameters, compiled in **Table 1** and their XPS determined surface chemical composition, shown in **Table 2**, however, suggests a much stronger influence of the particle preparation than their size on the chemical composition. Namely, calcination resulted in higher CuO content (TM17 vs TM18), while hydrazine was shown as a better reductant than H_2 in methanol (TM9 vs TM17) and in water (TM10 vs TM19)

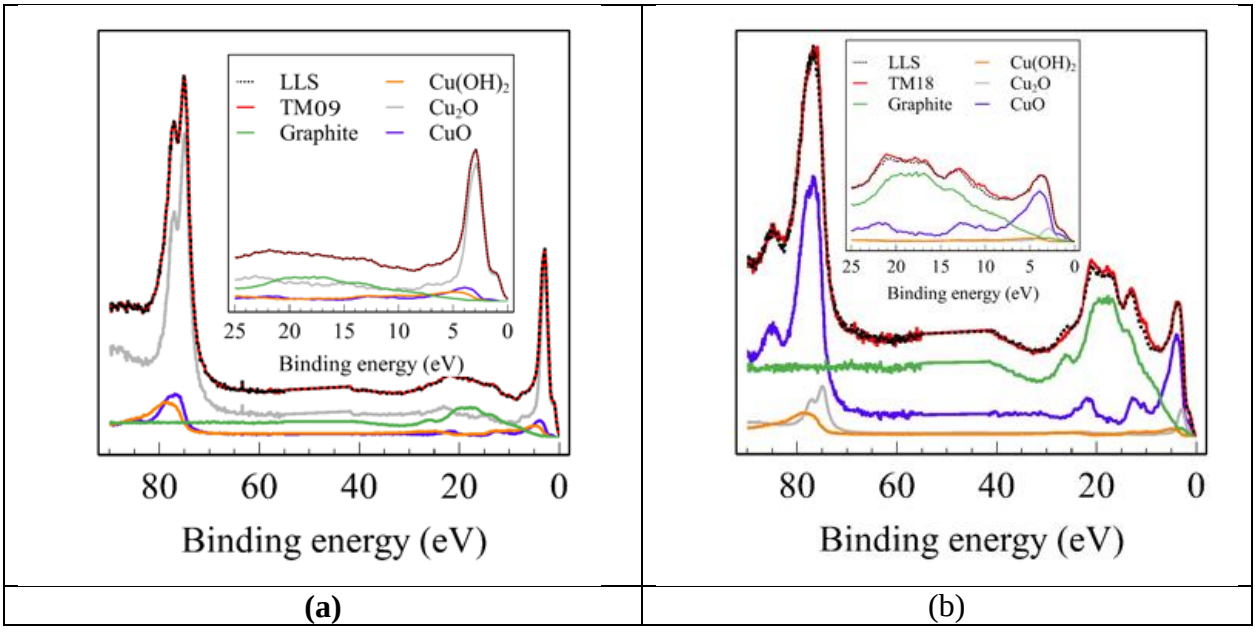

(a) (b)

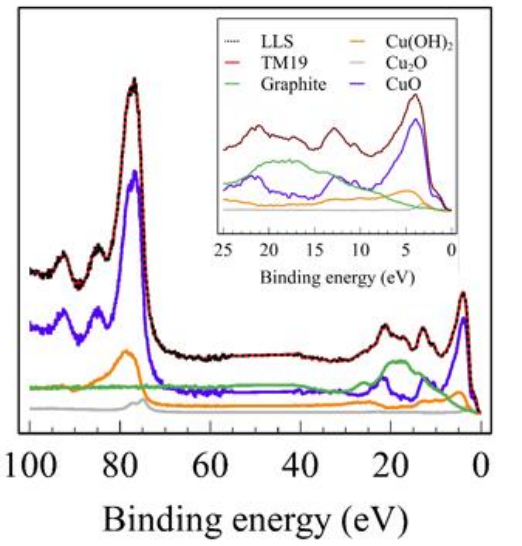

(c)

Figure 6. (a)-(c) Spectra formed from the sum of a set of four spectra representing graphite, Cu_2O, CuO and $Cu(OH)_2$ appropriately scaled to reproduce an experimental spectrum measured from samples TM09, TM18 and TM19. LSS spectra are shown in black and in most cases, it overlaps with the experimental.

Table 2. Analysis of chemical state for a range of Cu NP/graphite samples based on component spectra shown in **Figure 5** and **6**. Percent area is based on signal above a Tougaard background applied to Cu 3p signal.

Sample Identifier	$Cu(OH)_2$ %	Cu_2O %	CuO %
TM07	20.1	42.6	37.3
TM09	14.9	69.5	15.6
TM10	18.4	51.8	29.7
TM15	9.8	13.8	76.4
TM17	83.7	0.6	15.7
TM18	8.9	10.2	80.8
TM19	22.6	2.8	74.6

3.4. Evolution of copper nanoparticles supported on graphite under X-rays: effect of the measurements on the chemical state of copper. An IASM approach is based on sample knowledge and the manipulation of data acquired from the samples of interest. Treating spectra as vectors, data are transformed to new spectral forms from the original measured data by a combination of observing similarities to standard materials spectra from other sources (such as the La Trobe XPS database) [46] and observing relationships between photoemission peaks from the data under analysis as these transformations are performed.

Data sets corresponding to Cu NP/graphite exhibiting Cu(II) characteristics were selected for further analysis. A sequence of repetitive measurements was performed for the sample identified as TM15. The objective for these repeat measurements of TM15 was to assess the

stability of these materials with respect to the measurement process. These repeat measurements provide useful information about reduced states for the Cu NP/graphite.

IASM transformation was applied to all data collected from each sample to include Cu 2p, Cu Auger, O 1s, C 1s, Cu 3p and valance band narrow scan spectra. Data are measured using pass energy, 20 hybrid transfer lens mode slot selected area aperture and slot entrance aperture to the hemispherical analyzer on a Kratos Axis Ultra. Irregular energy increments were used to permit extended energy intervals for Cu Auger and other nominal background intervals used to provide context for photoemission signal acquired at a smaller energy step size suitable for peak widths achieved for pass energy 20/slot energy resolution. Vectors formed from these merged narrow-scan signal are processed to remove a U 2 Tougaard background where C = -1643 (Equation (2) as proposed by Tougaard for a universal background to photoemission spectra). While computing spectroscopic shapes representative of CuO, Cu_2O and $Cu(OH)_2$ peaks were included in the calculation allowing variations in carbon, Cu 3p and valance band data to be examined. By monitoring changes to these contextual peaks relationships of importance to the chemistry of interest are assessed and help guide the selection of appropriate intermediate forms. The exercise of computing these intermediate spectral shapes provides insight into the potential chemistry of these materials under analysis and is seen as valuable in its own right. Cu metal and Cu(I) are difficult to separate using Cu 2p, however making use of Cu Auger and O 1s it is clear the component assigned to Cu_2O includes oxygen signal and the shape for the corresponding Cu Auger assigned as Cu(I) is clearly not Cu metal Auger (not shown). Both Cu 2p and Cu Auger generate trends within the TM15 stability study shown in **Figure 7c**, namely, the component assigned as Cu(I) increases with elapsed time while both CuO and $Cu(OH)_2$ decrease with time.

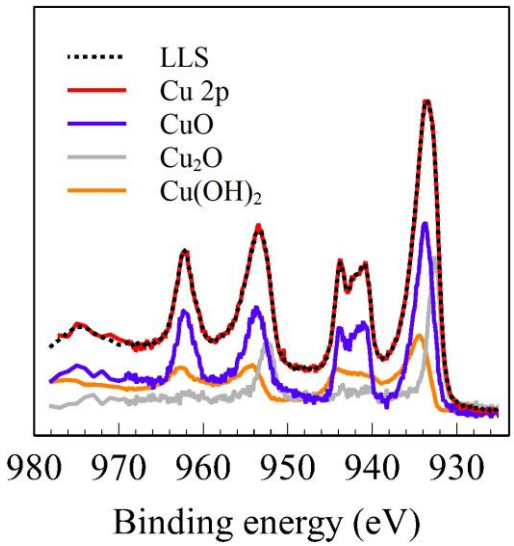

(a) Linear Least Squares decomposition of TM15 Cu 2p after 523 seconds of elapsed time during sample stability study.

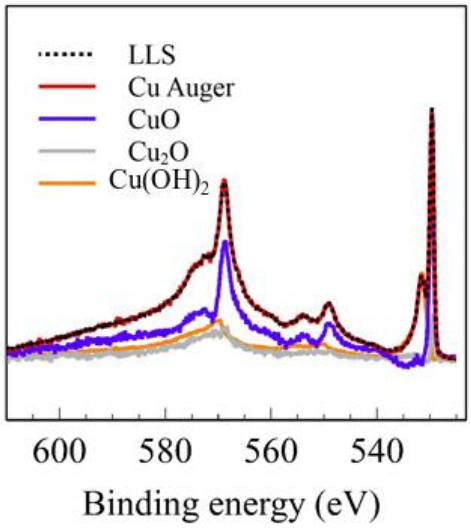

(b) Linear Least Squares decomposition of TM15 Cu Auger and O 1s after 523 seconds of elapsed time during sample stability study.

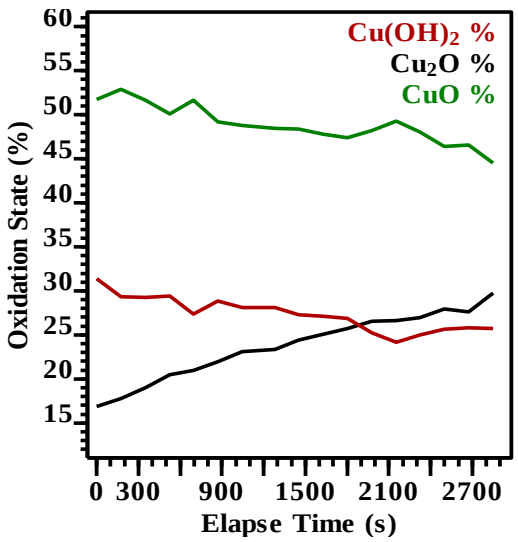

(c) Linear Least Squares decomposition of TM15 Cu 2p profiling the response of Cu NP/graphite to acquisition conditions plotted against elapsed time between measurements.

Figure 7.

Spectral forms in **Figure 7** evolved with elapsed time under the X-ray beam and LLS applied to these data based on IASM approach indicated the measured proportion for Cu_2O increased as CuO and $Cu(OH)_2$. XPS is a surface sensitive technique so these changes could be due to changes in chemistry or segregation of particles. A similar analysis based on valence band region peaks indicates attenuation of graphite signal as a proportion with time; therefore, segregation is a distinct possibility as graphite is not expected to change its chemical state. Finally, there is also the possibility the sample is being contaminated by a carbon overlayer

which increases with time. Nevertheless, these results illustrate how an analysis based on IASM is sensitive to changes in sample composition and capable of measuring small changes in surface chemistry. We, therefore, treat the composition **Table 2** for as received TM15, TM17, TM18 and TM19 with caution since the contribution from Cu(I) may be influenced by the XPS measurement itself.

An intriguing question arises whether XPS databases, such as XPSSurfA [46], The La Trobe University, Australia, XPS Reference Dataset based on the crowdsourcing of various XPS spectra, can be utilized in combination with IASM. Availability of spectra in a widely used file format (VAMAS ISO 14976) is of great value when assessing IASM component shapes and was extensively used in the preparation of this paper and other analyses using IASM. However, the key to using the IASM approach is to make use of consistent data sets measured from samples with similar characteristics. This necessarily means data acquired from different instruments from samples with potentially different handling, storage, preparation include differences in intensities that make it difficult to predict and make use of when fitting by LLS. Fitting of unknown data by linear least squares requires pre-processing steps aimed at aligning data from different samples from different instruments and these pre-processing steps return user bias into data treatment. The TM15 degradation study provides an example of why IASM is so powerful when attempting to understand samples. If CuO component has a shape with a proportion of Cu_2O, it can appear that the Cu_2O is only anticorrelated with the $Cu(OH)_2$. Only if CuO shape is correct then there is the possibility to see both CuO and $Cu(OH)_2$ decline with the exposure time, as shown in **Figure 7**. Hence, the most appropriate method is to measure fitting components and sample of interest on the same instrument, potentially deriving them by applying sample modifiers, such as X-ray exposure, temperature or oxidizing/reducing gases, currently achievable using near ambient pressure instruments.

4. Conclusions. The research was performed into managing the problem of operator bias in describing complex metal, such as Cu 2p, spectral envelopes by acquiring well-formed photoemission peaks with lab-based instruments and creating line shapes capable to characterizing these well-formed data. An XPS data processing technique for extracting line-shapes from experimental data based on a vector model has been developed and found to provide valuable insights into changes induced in Cu NP/graphite. In particular, components of Cu NP/graphite were constructed from the data rather than using synthetic components. It was illustrated that Cu 3p and VB data support the assignment of Cu_2O rather than Cu metal

and allow for direct quantification of each spectral component weight in the overall surface composition. Examples of the potential IASM application are not limited to copper and are abound. For example, recent data by David J. Morgan elucidated ruthenium containing catalyst chemical speciation using Ru 3p region for determination of Ru oxidation state rather than conventionally used Ru 3d. Innate photoreduction of $RuCl_3$ was shown to take place when exposed to X-rays while also undergoing complex surface hydrolysis due to the intrinsic sample hygroscopicity [47]. These changes in the sample physical state should be encouraged and measured and the corresponding line shapes can potentially be used to reconstruct the overall sample surface composition. Thus, we believe that the emergence of NAP-XPS will allow routinely generating sample modifiers needed to accurately interpret complex spectral envelopes.

5. Acknowledgments. This work by J.B. was supported as part of UNCAGE-ME, an Energy Frontier Research Center funded by the U.S. Department of Energy, Office of Science, Basic Energy Sciences under Award No. DE-SC0012577.

6. Supplemental material contains numerical data and references used to construct Figure 1.

References

[1] D.R. Baer, M.H. Engelhard, XPS analysis of nanostructured materials and biological surfaces, J. Electron Spectros. Relat. Phenomena. 178–179 (2010) 415–432. doi:10.1016/j.elspec.2009.09.003.

[2] M.C. Biesinger, C. Brown, J.R. Mycroft, R.D. Davidson, N.S. McIntyre, X-ray photoelectron spectroscopy studies of chromium compounds, Surf. Interface Anal. 36 (2004) 1550–1563. doi:10.1002/sia.1983.

[3] M.C. Biesinger, B.P. Payne, L.W.M. Lau, A. Gerson, R.S.C. Smart, X-ray photoelectron spectroscopic chemical state quantification of mixed nickel metal, oxide and hydroxide systems, Surf. Interface Anal. 41 (2009) 324–332. doi:10.1002/sia.3026.

[4] A.P. Grosvenor, M.C. Biesinger, R.S.C. Smart, N.S. McIntyre, New interpretations of XPS spectra of nickel metal and oxides, Surf. Sci. 600 (2006) 1771–1779. doi:https://doi.org/10.1016/j.susc.2006.01.041.

[5] M.C. Biesinger, L.W.M. Lau, A.R. Gerson, R.S.C. Smart, Resolving surface chemical states in XPS analysis of first row transition metals, oxides and hydroxides: Sc, Ti, V, Cu and Zn, Appl. Surf. Sci. 257 (2010) 887–898. doi:https://doi.org/10.1016/j.apsusc.2010.07.086.

[6] A.P. Grosvenor, B.A. Kobe, M.C. Biesinger, N.S. McIntyre, Investigation of multiplet splitting of Fe 2p XPS spectra and bonding in iron compounds, Surf. Interface Anal. 36 (2004) 1564–1574. doi:10.1002/sia.1984.

[7] M.C. Biesinger, B.P. Payne, A.P. Grosvenor, L.W.M. Lau, A.R. Gerson, R.S.C. Smart, Resolving surface chemical states in XPS analysis of first row transition metals, oxides and hydroxides: Cr, Mn, Fe, Co and Ni, Appl. Surf. Sci. 257 (2011) 2717–2730. doi:https://doi.org/10.1016/j.apsusc.2010.10.051.

[8] Neal Fairley, XPS lineshapes and curve fitting, in: D. Briggs, J.T. Grant (Eds.), Surf. Anal. by Auger X-Ray Photoelectron Spectrosc., SurfaceSpectra Ltd and IM Publications, Chichester, UK, 2003: pp. 397–420.

[9] D.O. Scanlon, G.W. Watson, D.J. Payne, G.R. Atkinson, R.G. Egdell, D.S.L. Law, Theoretical and Experimental Study of the Electronic Structures of MoO 3 and MoO 2, J. Phys. Chem. C. 114 (2010) 4636–4645. doi:10.1021/jp9093172.

[10] J. Baltrusaitis, B. Mendoza-Sanchez, V. Fernandez, R. Veenstra, N. Dukstiene, A. Roberts, N. Fairley, Generalized molybdenum oxide surface chemical state XPS determination via informed amorphous sample model, Appl. Surf. Sci. 326 (2015) 151–161. doi:10.1016/j.apsusc.2014.11.077.

[11] B.N. Reinecke, K.P. Kuhl, H. Ogasawara, L. Li, J. Voss, F. Abild-Pedersen, A. Nilsson, T.F. Jaramillo, Elucidating the electronic structure of supported gold nanoparticles and its relevance to catalysis by means of hard X-ray photoelectron spectroscopy, Surf. Sci. 650 (2016) 24–33. doi:10.1016/j.susc.2015.12.025.

[12] R.S. Rao, R.T.K. Baker, M.A. Vannice, Furfural hydrogenation over carbon- supported copper, Catal. Letters. 60 (1999) 51–57.

doi:10.1023/A:1019090520407.

[13] R. Kas, R. Kortlever, A. Milbrat, M.T.M. Koper, G. Mul, J. Baltrusaitis, Electrochemical CO2 reduction on Cu2O-derived copper nanoparticles: controlling the catalytic selectivity of hydrocarbons., Phys. Chem. Chem. Phys. 16 (2014) 12194–12201. doi:10.1039/c4cp01520g.

[14] E. V. Kondratenko, G. Mul, J. Baltrusaitis, G.O. Larrazábal, J. Pérez-Ramírez, Status and perspectives of CO2 conversion into fuels and chemicals by catalytic, photocatalytic and electrocatalytic processes, Energy Environ. Sci. 6 (2013) 3112. doi:10.1039/c3ee41272e.

[15] H. Mistry, A.S. Varela, C.S. Bonifacio, I. Zegkinoglou, I. Sinev, Y.-W. Choi, K. Kisslinger, E.A. Stach, J.C. Yang, P. Strasser, B.R. Cuenya, Highly selective plasma-activated copper catalysts for carbon dioxide reduction to ethylene, Nat. Commun. 7 (2016) 12123. doi:10.1038/ncomms12123.

[16] C.S. Chen, A.D. Handoko, J.H. Wan, L. Ma, D. Ren, B.S. Yeo, Stable and selective electrochemical reduction of carbon dioxide to ethylene on copper mesocrystals, Catal. Sci. Technol. 5 (2015) 161–168. doi:10.1039/C4CY00906A.

[17] K.L. Deutsch, B.H. Shanks, Active species of copper chromite catalyst in C–O hydrogenolysis of 5-methylfurfuryl alcohol, J. Catal. 285 (2012) 235–241. doi:10.1016/j.jcat.2011.09.030.

[18] W. Taifan, J.-F. Boily, J. Baltrusaitis, Surface chemistry of carbon dioxide revisited, Surf. Sci. Rep. 71 (2016) 595–671. doi:10.1016/j.surfrep.2016.09.001.

[19] J. Knudsen, J.N. Andersen, J. Schnadt, A versatile instrument for ambient pressure x-ray photoelectron spectroscopy: The Lund cell approach, Surf. Sci. 646 (2016) 160–169. doi:10.1016/j.susc.2015.10.038.

[20] M. Salmeron, R. Schlogl, Ambient pressure photoelectron spectroscopy: A new tool for surface science and nanotechnology, Surf. Sci. Rep. 63 (2008) 169–199. doi:10.1016/j.surfrep.2008.01.001.

[21] J. Dou, Z. Sun, A.A. Opalade, N. Wang, W. Fu, F. (Feng) Tao, Operando chemistry of catalyst surfaces during catalysis, Chem. Soc. Rev. 46 (2017) 2001–2027. doi:10.1039/C6CS00931J.

[22] M. Salmeron, From Surfaces to Interfaces: Ambient Pressure XPS and Beyond, Top. Catal. 61 (2018) 2044–2051. doi:10.1007/s11244-018-1069-0.

[23] A.Y. Klyushin, T.C.R. Rocha, M. Hävecker, A. Knop-Gericke, R. Schlögl, A near ambient pressure XPS study of Au oxidation, Phys. Chem. Chem. Phys. 16 (2014) 7881. doi:10.1039/c4cp00308j.

[24] H. Ali-Löytty, M.W. Louie, M.R. Singh, L. Li, H.G. Sanchez Casalongue, H. Ogasawara, E.J. Crumlin, Z. Liu, A.T. Bell, A. Nilsson, D. Friebel, Ambient-Pressure XPS Study of a Ni–Fe Electrocatalyst for the Oxygen Evolution Reaction, J. Phys. Chem. C. 120 (2016) 2247–2253. doi:10.1021/acs.jpcc.5b10931.

[25] F. (Feng) Tao, Operando Studies of Catalyst Surfaces during Catalysis and under Reaction Conditions: Ambient Pressure X-Ray Photoelectron Spectroscopy with a

Flow-Cell Reactor, ChemCatChem. 4 (2012) 583–590. doi:10.1002/cctc.201200002.

[26] L. Nguyen, F.F. Tao, Y. Tang, J. Dou, X.-J. Bao, Understanding Catalyst Surfaces during Catalysis through Near Ambient Pressure X-ray Photoelectron Spectroscopy, Chem. Rev. 119 (2019) 6822–6905. doi:10.1021/acs.chemrev.8b00114.

[27] C.H. Wu, B. Eren, H. Bluhm, M.B. Salmeron, Ambient-Pressure X-ray Photoelectron Spectroscopy Study of Cobalt Foil Model Catalyst under CO, H 2 , and Their Mixtures, ACS Catal. 7 (2017) 1150–1157. doi:10.1021/acscatal.6b02835.

[28] S. Kaya, H. Ogasawara, L.-Å. Näslund, J.-O. Forsell, H.S. Casalongue, D.J. Miller, A. Nilsson, Ambient-pressure photoelectron spectroscopy for heterogeneous catalysis and electrochemistry, Catal. Today. 205 (2013) 101–105. doi:10.1016/j.cattod.2012.08.005.

[29] A.R. Head, H. Bluhm, Ambient Pressure X-Ray Photoelectron Spectroscopy, in: K.B.T.-E. of I.C. Wandelt (Ed.), Ref. Modul. Chem. Mol. Sci. Chem. Eng., Elsevier, Oxford, 2016: pp. 13–27. doi:10.1016/B978-0-12-409547-2.10924-2.

[30] R. Mom, L. Frevel, J.-J. Velasco-Vélez, M. Plodinec, A. Knop-Gericke, R. Schlögl, The Oxidation of Platinum under Wet Conditions Observed by Electrochemical X-ray Photoelectron Spectroscopy, J. Am. Chem. Soc. 141 (2019) 6537–6544. doi:10.1021/jacs.8b12284.

[31] Q. Liu, Y. Han, J. Cai, E.J. Crumlin, Y. Li, Z. Liu, CO2 Activation on Cobalt Surface in the Presence of H2O: An Ambient-Pressure X-ray Photoelectron Spectroscopy Study, Catal. Letters. 148 (2018) 1686–1691. doi:10.1007/s10562-018-2362-z.

[32] P.M.A. Sherwood, The use and misuse of curve fitting in the analysis of core X- ray photoelectron spectroscopic data, Surf. Interface Anal. 51 (2019) 589–610. doi:10.1002/sia.6629.

[33] M. d'Halluin, T. Mabit, N. Fairley, V. Fernandez, M.B. Gawande, E. Le Grognec, F.-X. Felpin, Graphite-supported ultra-small copper nanoparticles – Preparation, characterization and catalysis applications, Carbon N. Y. 93 (2015) 974–983. doi:10.1016/j.carbon.2015.06.017.

[34] D.O. Scanlon, B.J. Morgan, G.W. Watson, A. Walsh, Acceptor Levels in p-Type Cu2O: Rationalizing Theory and Experiment, Phys. Rev. Lett. 103 (2009) 096405. doi:10.1103/PhysRevLett.103.096405.

[35] M.P. Seah, I.S. Gilmore, S.J. Spencer, XPS: binding energy calibration of electron spectrometers 4-assessment of effects for different x-ray sources, analyser resolutions, angles of emission and overall uncertainties, Surf. Interface Anal. 26 (1998) 617–641. doi:10.1002/(SICI)1096-9918(199808)26:9<617::AID-SIA407>3.0.CO;2-V.

[36] M.P. Seah, I.S. Gilmore, G. Beamson, XPS: binding energy calibration of electron spectrometers 5-re-evaluation of the reference energies, Surf. Interface Anal. 26 (1998) 642–649. doi:10.1002/(SICI)1096-9918(199808)26:9<642::AID-SIA408>3.0.CO;2-3.

[37] S. Tougaard, Practical algorithm for background subtraction, Surf. Sci. 216 (1989) 343–360. doi:10.1016/0039-6028(89)90380-4.

[38] S. Béchu, M. Richard-Plouet, V. Fernandez, J. Walton, N. Fairley, Developments in

numerical treatments for large data sets of XPS images, Surf. Interface Anal. 48 (2016) 301–309. doi:10.1002/sia.5970.

[39] M.P. Seah, Simple universal curve for the energy-dependent electron attenuation length for all materials, Surf. Interface Anal. 44 (2012) 1353–1359. doi:10.1002/sia.5033.

[40] M. Prutton, M.M. El Gomati, Scanning Auger Electron Microscopy, Wiley, 2005. doi:10.1002/9780470866795.

[41] J.H. Scofield, Hartree-Slater subshell photoionization cross-sections at 1254 and 1487 eV, J. Electron Spectros. Relat. Phenomena. 8 (1976) 129–137. doi:10.1016/0368-2048(76)80015-1.

[42] S. Tanuma, C.J. Powell, D.R. Penn, Calculations of electron inelastic mean free paths. IX. Data for 41 elemental solids over the 50 eV to 30 keV range, Surf. Interface Anal. 43 (2011) 689–713. doi:10.1002/sia.3522.

[43] C.J. Powell, The energy dependence of electron inelastic mean free paths, Surf. Interface Anal. 10 (1987) 349–354. doi:10.1002/sia.740100707.

[44] C.-K. Wu, M. Yin, S. O'Brien, J.T. Koberstein, Quantitative Analysis of Copper Oxide Nanoparticle Composition and Structure by X-ray Photoelectron Spectroscopy, Chem. Mater. 18 (2006) 6054–6058. doi:10.1021/cm061596d.

[45] C.C. Chusuei, M.A. Brookshier, D.W. Goodman, Correlation of Relative X-ray Photoelectron Spectroscopy Shake-up Intensity with CuO Particle Size, Langmuir. 15 (1999) 2806–2808. doi:10.1021/la9815446.

[46] A.J. Barlow, R.T. Jones, A.J. McDonald, P.J. Pigram, XPSSurfA: An open collaborative XPS data repository using the CMSShub platform, Surf. Interface Anal. 50 (2018) 527–540. doi:10.1002/sia.6417.

[47] D.J. Morgan, Resolving ruthenium: XPS studies of common ruthenium materials, Surf. Interface Anal. 47 (2015) 1072–1079. doi:10.1002/sia.5852.

Graphical abstract